HOKKAIDO UNIVERSITY

Title	Significant effects of epitaxial strain on the nonlinear transport properties in Ca2RuO4 thin films with the current-driven transition
Author(s)	Tsubaki, Keiji; Arita, Masashi; Katase, Takayoshi et al.
Citation	Japanese Journal of Applied Physics, 63(1), 01SP03 https://doi.org/10.35848/1347-4065/acf2a3
Issue Date	2023-12-15
Doc URL	https://hdl.handle.net/2115/93770
Rights	This is the Accepted Manuscript version of an article accepted for publication in Japanese Journal of Applied Physics(JJAP). IOP Publishing Ltd is not responsible for any errors or omissions in this version of the manuscript or any version derived from it. The Version of Record is available online at http://doi.org/10.35848/1347-4065/acf2a3.
Rights(URL)	https://creativecommons.org/licenses/by-nc-nd/4.0/
Type	journal article
File Information	Tsubaki_2024_Jpn._J._Appl._Phys.pdf

Hokkaido University Collection of Scholarly and Academic Papers : HUSCAP

Significant effects of epitaxial strain on the nonlinear transport properties in Ca_2RuO_4 thin films with the current-driven transition

Keiji Tsubaki[1]*, Masashi Arita[2], Takayoshi Katase[3], Toshio Kamiya[3], Atsushi Tsurumaki-Fukuchi[2]*, and Yasuo Takahashi[2]

[1]*Graduate School of Information Science and Technology, Hokkaido University, Sapporo 060-0814, Japan*

[2]*Faculty of Information Science and Technology, Hokkaido University, Sapporo 060-0814, Japan*

[3]*MDX Research Center for Element Strategy, International Research Frontiers Initiative, Tokyo Institute of Technology, Yokohama, 226-8503 Japan*

E-mail: tsubaki_guitar48@eis.hokudai.ac.jp, a.fukuchi@ist.hokudai.ac.jp

Control of the nonlinear transport properties in strongly correlated materials with metal–insulator transitions has become an important task in the development of next-generation computing elements. Here, we demonstrate that the nonlinear transport properties in the Mott insulator Ca_2RuO_4, which are caused by the current-driven transition with a nonthermal-type mechanism, can be significantly affected by epitaxial strain in thin films. Ca_2RuO_4 epitaxial thin films were grown on various single-crystal substrates by the solid-phase epitaxy method under nonvacuum conditions, and the effects of epitaxial strain on the transport properties were investigated. While nonlinear transport properties with negative differential resistance behavior were observed in [001]-oriented $Ca_2RuO_4/LaAlO_3$ (001) thin films, the current transport nonlinearity was critically diminished in the current–voltage characteristics of $Ca_2RuO_4/NdCaAlO_4$ (100) thin films with the [110] orientation. Through structural characterization of the thin films, a possible correlation between the strain states and nonlinear transport properties was discussed.

1. Introduction

Toward the development of beyond CMOS and non-von Neumann computing technologies, increasing interest has been focused on application of strongly correlated and quantum materials to novel computing elements in recent years. Materials with metal–insulator phase transitions have been considered particularly promising for device applications because of the highly reliable high-operation-speed conductivity changes in the materials driven by the transitions.[1,2] By applying electric fields or injecting currents, a variety of nonlinear transport properties have been demonstrated in the materials with metal–insulator transitions,[3-21] and important application functions have been derived from the transport nonlinearity. In principle, materials with metal–insulator phase transitions show sharp resistive switching[4,5,8,10,12,14,17,18,20-23] and negative differential resistance (NDR)[3-11,13-23] behavior in the current–voltage characteristics when measurements are conducted under voltage- and current-sweeping conditions, respectively. Using resistive switching and NDR characteristics as driving principles, promising functional devices such as Mott memristors,[1,2,23] Mott artificial neurons,[1,8,17] and Mott oscillators[1,4,8,17,18,20] have been proposed and demonstrated in previous studies.

To achieve practical operation of these devices with such functionalities, many attempts to control the nonlinear transport properties (switching and NDR) in metal–insulator transition materials have recently been made,[11,17,19,20] but the demonstrated controllability is currently limited. Previous studies have revealed that the limited controllability of the nonlinear transport phenomena is mainly attributable to the induction mechanisms predominated by Joule heating.[7,11,16-20] In materials that show clear temperature-induced metal–insulator transitions (such as VO_2), the nonlinear transport phenomena in the current–voltage characteristics have been reported to be dominantly caused by the temperature-driven transitions in most cases, which are triggered by filamentary thermal runaway in the materials via Joule self-heating.[7,16,18-20] The current–voltage characteristics are thus generally discontinuous, and the nonlinear transport properties in the materials are generally hard to control because of the difficulty in controlling the abrupt thermal runaway.

Recently, a different class of metal–insulator transitions has been demonstrated in some kinds of strongly correlated materials, *i.e.*, current-driven metal–insulator transitions, in which the current density acts as an intrinsic control parameter of the transitions.[24] The layered orthorhombic perovskite Ca_2RuO_4 is known as a representative platform for this class of metal–insulator transitions.[5,6,9,10,12-15,21,25] In the current–voltage characteristics of Ca_2RuO_4, clear nonlinear transport phenomena (both switching and NDR) have been

observed based on the current-driven transition,[5,6,9,10,12-15,21] and because of the nonthermal origin of the transition, the driving mechanisms have been indicated to be not predominated by thermal runaway due to Joule heating but by current injection itself,[9,14,21] unlike those in materials such as VO_2. In the nonlinear transport phenomena, additionally, previous studies have demonstrated that the crystal lattice dimensions of Ca_2RuO_4 progressively and continuously change with current injection (and with progression of the current-induced transition), originating from the strong electron-lattice coupling in the material.[10,24,25] These results suggest that the nonlinear transport properties in Ca_2RuO_4 possibly have higher characteristic controllability compared to the properties based on temperature-induced transitions, and the nonlinearity may be reliably controllable using the strain states in the material, particularly in thin films under epitaxial strain. However, the actual effects of structural strain on the nonlinear transport properties have not yet been elucidated for Ca_2RuO_4.

In this study, we grew Ca_2RuO_4 epitaxial thin films on single-crystal substrates with various lattice dimensions and measured the resistivity–temperature and current–voltage characteristics in detail to reveal the impacts of epitaxial strain on the nonlinear transport properties. The measurements indicated that the nonlinearity of the current–voltage characteristics nearly completely disappeared in [110]-oriented Ca_2RuO_4/$NdCaAlO_4$ (100) epitaxial thin films, whereas clear NDR behavior was observed in [001]-oriented epitaxial films of Ca_2RuO_4/$LaAlO_3$ (001). Significant effects of epitaxial strain on the nonlinear transport properties were demonstrated by the measurements, and important insights into the future development of Mott computing devices were provided.

2. Experimental methods

While the current-induced metal–insulator transition of Ca_2RuO_4 is generally hardly observed in epitaxial thin films grown by vacuum deposition methods such as pulsed laser deposition,[26-30] we have recently shown that the current-induced transition becomes observable in nonvacuum-grown epitaxial films with increased resistivity of Ca_2RuO_4, which were grown by solid phase epitaxy at atmospheric pressure.[12,21] The Ca_2RuO_4 thin films examined in this study were thus grown by the nonvacuum solid-phase epitaxy technique on various substrate materials, and the substrate effects on the crystal structures and nonlinear transport properties were investigated. In this study, 100 nm-thick Ca_2RuO_4 thin films were grown on single-crystal substrates of $YAlO_3$ (001), $LaAlO_3$ (001), $LaSrGaO_4$ (001), $NdGaO_3$ (110), LSAT (100), and $NdCaAlO_4$ (100). We first fabricated amorphous

Ca_2RuO_x precursor thin films on the above six kinds of substrates by pulsed laser deposition, and then the solid-phase epitaxial growth of the Ca_2RuO_4 thin films was conducted from the precursor films at a growth temperature of 1300 °C in an Ar (99%) + O_2 (1%) atmosphere with a pressure of 1.0 atm, as described in our previous papers.[12,21] Prior to precursor deposition, the $YAlO_3$ (001) and $LaAlO_3$ (001) substrates were etched with concentrated HCl solutions, and the other substrates were preannealed at 1300 °C (the same conditions as for the film growth) to form atomically flat step-and-terrace structures on their surfaces.[31-33] The crystal structures and surface morphologies of the Ca_2RuO_4 thin films were analyzed by X-ray diffraction (XRD) and atomic force microscopy using a SmartLab (Rigaku), a D8 Discover (Bruker AXS Inc.) and a NanoCute (Hitachi High-Tech Co.). The resistivity–temperature characteristics of the Ca_2RuO_4 thin films were measured by the four-probe method using the physical property measurement system (PPMS, Quantum Design). For the measurements of the current–voltage characteristics of the films, in-plane two-terminal electrodes of Au (100 nm)/Cr (5 nm) with an electrode gap of 20 μm were fabricated on the Ca_2RuO_4 thin films by vacuum evaporation and standard photolithography processes. The detailed configurations of the in-plane electrodes were described in our previous papers.[12,21] The current–voltage measurements of the Ca_2RuO_4 thin films were conducted at stage temperatures of 20–590 K in a cryogenic probe station system (Nagase, GRAIL-20-305-6-LV) and a high-temperature probe station system using a semiconductor parameter analyzer (Keysight 4156C).

3. Results and discussion

The crystal lattice dimensions reported for bulk Ca_2RuO_4 and the substrate materials used in this study are summarized in Table I. Bulk Ca_2RuO_4 undergoes the temperature-induced metal–insulator transition at the transition temperature of 357 K, with accompanying significant changes in the crystal structure, which are characterized by large shrinkage/elongation of the RuO_6 octahedron in the *c*-axis direction.[34-36] The ranges of the possible lattice mismatches between the insulating (shorter *c*-axis length, for $T < 357$ K) phase of bulk Ca_2RuO_4 and the substrate materials, determined as $(d_{CRO} - d_{sub})/d_{CRO} \times 100$ [%], where d_{CRO} and d_{sub} are the in-plane lattice dimensions of bulk Ca_2RuO_4 (in the insulating phase at room temperature) and the substrate, are also shown in Table I. Note that in the table, hypothetical pseudo-K_2NiF_4 structures, where d_{CRO} in the *ab* plane is transformed as $d_{CRO}/\sqrt{2}$ from the original orthorhombic lattice, are assumed for the lattice dimensions of bulk Ca_2RuO_4, and a pseudocubic notation is used for the dimensions of

$YAlO_3$ (001), $LaAlO_3$ (001), and $NdGaO_3$ (110) to make direct comparisons between them. In the high-temperature solid-phase epitaxial growth of Ca_2RuO_4 conducted in this study, we observed that the crystal and phase structures of the grown films are critically influenced by the chemical stability of the substrate materials and the lattice mismatch. The results of the epitaxial growth trials of Ca_2RuO_4 are displayed in the right column of Table I, which were determined based on XRD analyses. In the present study, two tendencies for the solid-phase epitaxial growth of Ca_2RuO_4 were suggested from the structure characterizations: (1) aluminate substrates ($YAlO_3$, $LaAlO_3$, and $NdCaAlO_4$) have a higher chemical stability against interfacial reactions with Ca_2RuO_4 than gallate and tantalate substrates ($LaSrGaO_4$, $NdGaO_3$, and LSAT), and (2) pseudocubic substrates ($YAlO_3$, $LaAlO_3$, and $NdGaO_3$) have a higher chemical stability than K_2NiF_4-structured tetragonal substrates ($LaSrGaO_4$ and $NdCaAlO_4$). In the growth experiments conducted in this study, we confirmed that impurity-free Ca_2RuO_4 thin films could not be obtained on $LaSrGaO_4$ (001) and LSAT (100) substrates at a growth temperature of 1300 °C because of their interfacial reactivity with Ca_2RuO_4 and resultant impurity phase formation (Table I). Meanwhile, $YAlO_3$ (001) substrates were considered to have sufficient chemical stability against interfacial reactions with Ca_2RuO_4, similar to the chemically analogous material $LaAlO_3$ (001). However, phase-pure Ca_2RuO_4 thin films also could not be grown on $YAlO_3$ (001) substrates by this growth method, probably due to their relatively large crystal lattice mismatch with bulk Ca_2RuO_4 (Table I). As a result, the growth of nearly phase-pure Ca_2RuO_4 epitaxial thin films was achieved on the three kinds of substrates of $LaAlO_3$ (001), $NdGaO_3$ (110), and $NdCaAlO_4$ (100) in the present study, as indicated in Table I.

Out-of-plane XRD patterns measured under a θ–2θ scan for the Ca_2RuO_4 (100 nm)/$LaAlO_3$ (001), Ca_2RuO_4 (100 nm)/$NdGaO_3$ (110), and Ca_2RuO_4 (100 nm)/$NdCaAlO_4$ (100) thin films are shown in Figs. 1(a)–1(c). For the Ca_2RuO_4/$LaAlO_3$ (001) thin film, growth of a nearly phase-pure [001]-oriented Ca_2RuO_4 thin film was observed in the measurement, similar to our previous works.[12,21] Such apparently phase-pure [001]-oriented thin-film growth of Ca_2RuO_4 was also observed for Ca_2RuO_4/$NdGaO_3$ (110) in the XRD patterns (Fig. 1(b)). However, in the XRD measurements for Ca_2RuO_4/$NdGaO_3$ (110), additional satellite peaks were also reproducibly observed on the high-angle side of the substrate peaks (as marked by open circles in Fig. 1(b)) in multiple samples. As we will discuss later, these additional XRD reflections can be assigned to interfacial reactant layers at the Ca_2RuO_4/$NdGaO_3$ interface, which are unavoidably formed due to the relatively low chemical stability of $NdGaO_3$. For the Ca_2RuO_4/$NdCaAlO_4$ (100) thin films, growth of

phase-pure Ca_2RuO_4 films was also demonstrated in the XRD measurements (Fig. 1(c)). However, the measurements indicated that the $Ca_2RuO_4/NdCaAlO_4$ (100) thin films had a [110] orientation relative to the substrates (similar to the [100]-oriented growth of Ca_2RuO_4 thin films observed in $Ca_2RuO_4/NdCaAlO_4$ (110) [28]), unlike the $Ca_2RuO_4/LaAlO_3$ (001) and $Ca_2RuO_4/NdGaO_3$ (110) thin films. The in-plane twofold symmetry of the Ca_2RuO_4 lattice observed in the measurements under a ϕ scan (Fig. 1(d)) further supported the [110]-orientated growth of Ca_2RuO_4 in the $Ca_2RuO_4/NdCaAlO_4$ (100) thin films.

For the three kinds of nearly phase-pure Ca_2RuO_4 thin films of $Ca_2RuO_4/LaAlO_3$ (001), $Ca_2RuO_4/NdGaO_3$ (110), and $Ca_2RuO_4/NdCaAlO_4$ (100), the reciprocal space maps obtained by XRD measurements around the reflections from Ca_2RuO_4 are shown in Figs. 2(a)–2(d). Consistent with our previous investigations,[12] coherent epitaxial growth of the film on the substrate was observed for the $Ca_2RuO_4/LaAlO_3$ (001) film (Fig. 2(a)). The crystal lattice dimensions of the Ca_2RuO_4 thin film (in the original orthorhombic notation, determined by the reciprocal space maps) were $a = b = 0.536$ nm and $c = 1.216$ nm, where the in-plane lattice dimensions completely match the dimensions of $LaAlO_3$. The results indicated that the crystal lattice of the Ca_2RuO_4 thin film is elongated in the [001] direction compared to the insulating phase of bulk Ca_2RuO_4 (which has lattice dimensions of $a = 0.541$ nm, $b = 0.549$ nm, and $c = 1.196$ nm (Table I)) due to the compressive epitaxial strain applied from the $LaAlO_3$ (001) substrate (Fig. 2(e)). In the $Ca_2RuO_4/NdGaO_3$ (110) thin films, meanwhile, large broadening of the XRD reflections from Ca_2RuO_4 was observed in the in-plane [110] and [1−10] directions (which correspond to the [100] and [010] directions in the pseudo-K_2NiF_4 structure notation used in Table I) in the reciprocal space mapping (Fig. 2(b)). This result indicated that the Ca_2RuO_4 thin films on $NdGaO_3$ (110) do not have coherent lattice matching with the substrate lattice, whereas [001]-oriented nearly phase-pure film growth was demonstrated by the θ–2θ scan measurements (Fig. 1(b)). From the mapping, we can understand that epitaxial strain is not uniformly applied to the $Ca_2RuO_4/NdGaO_3$ (110) thin films from the substrates, although a c-axis length of 1.208 nm, which is not equal to the c-axis length of the bulk insulating phase of Ca_2RuO_4 (Table I), is obtained for the Ca_2RuO_4 thin film. We consider that the strong degradation of lattice matching in the $Ca_2RuO_4/NdGaO_3$ (110) thin films is possibly due to the formation of a small volume of interfacial reactant layer between Ca_2RuO_4 and $NdGaO_3$ (similar to the interfacial reactions observed in the $Ca_2RuO_4/LaSrGaO_4$ (001) thin films), which should have different in-plane lattice dimensions from both Ca_2RuO_4 and $NdGaO_3$, and the additional reflections observed in the θ–2θ scan measurements (Fig. 1(b)) are attributable to

the nonstoichiometric interfacial parts of the $NdGaO_3$ (110) substrate formed through the reactions. For the $Ca_2RuO_4/NdCaAlO_4$ (100) thin films, film-substrate lattice matching was selectively observed in the [001] direction of Ca_2RuO_4 from the reciprocal space mapping. As shown in Fig. 2(c), the *c*-axis length of the Ca_2RuO_4 film equivalently matched the *c*-axis length of $NdCaAlO_4$ in an in-plane direction, and a *c*-axis length of 1.212 nm (which is shorter than that of the $Ca_2RuO_4/LaAlO_3$ (001) thin films) was obtained for the Ca_2RuO_4 film lattice. In the in-plane [1−10] and [−110] directions, in contrast, lattice relaxation was observed for the films in the reciprocal space mapping (Fig. 2(d)). The *a*- and *b*-axis lengths of the $Ca_2RuO_4/NdCaAlO_4$ (100) films determined from the mapping are 0.532 and 0.534 nm, which do not coincide with the corresponding lattice dimensions of $NdCaAlO_4$ ($\sqrt{2}a = 5.21$ nm). The origin of the lattice relaxation in the [1−10] and [−110] directions can be directly attributed to the larger amounts of compressive lattice mismatch between the film and substrate in these directions (+3.7–+5.2%), which are significantly larger than the amount of tensile strain of −1.3% in the [001] direction. As a result, these measurements indicate that epitaxial strain in the $Ca_2RuO_4/NdCaAlO_4$ (100) thin films is anisotropically applied to the Ca_2RuO_4 lattice in the in-plane [001] direction, as illustrated in Fig. 2(f). We note that the epitaxial relationships and strain states observed in $Ca_2RuO_4/NdCaAlO_4$ (100) thin films are qualitatively similar to those reported for $Ca_2RuO_4/NdCaAlO_4$ (110) thin films fabricated by the pulsed laser deposition method.[28)]

The resistivity–temperature characteristics of the $Ca_2RuO_4/LaAlO_3$ (001), $Ca_2RuO_4/NdGaO_3$ (110), and $Ca_2RuO_4/NdCaAlO_4$ (100) thin films measured for 2.0 mm × 5.0 mm rectangular-shaped samples by the four-probe method are shown in Fig. 3(a). In the measurements, a difference of more than two orders of magnitude was observed between the resistivity of the $Ca_2RuO_4/LaAlO_3$ (001) thin film (0.2 Ω cm at 400 K) and those of the $Ca_2RuO_4/NdGaO_3$ (110) (70 Ω cm at 400 K) and $Ca_2RuO_4/NdCaAlO_4$ (100) (100 Ω cm at 400 K) thin films, while all the thin films showed a nonmetallic (semiconductor-like) temperature dependence of the resistivity with a negative temperature coefficient of resistivity (TCR, defined as $(1/\rho)(d\rho/dT)$) within the temperature range of 100–400 K (Fig. 3(b)). Note that for the $Ca_2RuO_4/NdGaO_3$ (110) and $Ca_2RuO_4/NdCaAlO_4$ (100) thin films, the resistivity could only be reliably measured for the limited temperature ranges of 290–400 K and 395–400 K because of the large resistivity amplitudes and the voltage limit of 95 mV set by the PPMS. The lower resistivity observed in the $Ca_2RuO_4/LaAlO_3$ (001) thin films is explained by considering the in-plane compressive strain from the $LaAlO_3$ (001) substrate (Fig. 2(e)), which decreases the energy splitting between the ($4d_{xz}$, $4d_{yz}$) and $4d_{xy}$ orbitals and

stabilizes the metallic phase of Ca_2RuO_4 (Table I), as discussed in earlier studies on the epitaxial films.[12,28-30] In contrast, the higher resistivity amplitudes observed in the $Ca_2RuO_4/NdGaO_3$ (110) thin films are attributable to the in-plane tensile strain from the $NdGaO_3$ (110) substrate (especially for the high-temperature metallic phase of Ca_2RuO_4 (Table I)), although the strain distributions are not uniform in the out-of-plane direction (Fig. 2(b)). In the $Ca_2RuO_4/NdCaAlO_4$ (100) thin films, where lattice relaxation is caused in the [1−10] direction of Ca_2RuO_4 but lattice matching occurs in the [001] direction (Fig. 2(f)), the effects of epitaxial strain on the resistivity are not straightforwardly understood. In the temperature range of the resistivity measurement (395–400 K), however, the epitaxial strain in the [001] direction is expected to in principle inhibit the growth of the metallic phase of Ca_2RuO_4 with a longer *c*-axis length of >1.225 nm[36] and to increase the resistivity from the value for the metallic phase, as previously discussed for $Ca_2RuO_4/NdCaAlO_4$ (110) epitaxial thin films.[28,29] Therefore, the resistivity of $>10^2$ Ω cm observed in the $Ca_2RuO_4/NdCaAlO_4$ (100) thin films is basically explained by considering the compressive epitaxial strain caused in the [001] direction.

The resistivity of the nonvacuum-grown $Ca_2RuO_4/LaAlO_3$ (001) thin films of the present study was 2–4 orders of magnitude higher than that reported for vacuum-grown $Ca_2RuO_4/LaAlO_3$ (001) epitaxial thin films,[26-30] similar to our previous observations.[12] In addition, the measurements in Fig. 3(a) demonstrate that this tendency is also applicable to the $Ca_2RuO_4/NdGaO_3$ (110) and $Ca_2RuO_4/NdCaAlO_4$ (100) thin films grown by the nonvacuum solid-phase epitaxy method. While the resistivity–temperature characteristics have only been examined in a limited number of studies, previous experiments have demonstrated that a $Ca_2RuO_4/NdGaO_3$ (110) thin film grown by the molecular beam epitaxy method has a resistivity of 0.6 Ω cm at 300 K,[30] and a $Ca_2RuO_4/NdCaAlO_4$ (110) thin film grown by the pulsed laser deposition method has a resistivity of 3.0 mΩ cm at 400 K,[29] which are much lower than the values observed in Fig. 3(a). Therefore, similar to the effects observed in the $Ca_2RuO_4/LaAlO_3$ (001) thin films,[12] we can assume that the resistivity–temperature characteristics of $Ca_2RuO_4/NdGaO_3$ (110) and $Ca_2RuO_4/NdCaAlO_4$ (100) thin films may be significantly affected by the internal Ru deficiency concentrations in Ca_2RuO_4, and the increased resistivity of the films in the present study may originate from the reduced Ru deficiency concentrations produced by the nonvacuum growth conditions.

Regarding the transition temperature of the temperature-induced metal–insulator transition, we have previously reported that the $Ca_2RuO_4/LaAlO_3$ (001) thin film has a transition temperature of 240 K, and the current-induced transition can be observed at

temperatures below 240 K, at which the high-resistivity phase will form in the Ca_2RuO_4 thin films.[12] In the $Ca_2RuO_4/NdGaO_3$ (110) and $Ca_2RuO_4/NdCaAlO_4$ (100) thin films of the present study, the transition temperatures are expected to be increased by the epitaxial strain effects from the bulk value (357 K) and to be >400 K. This assumption is based on the behavior of the resistivity–temperature characteristics (Fig. 3(a)), in which the resistivity is significantly higher than that of the metallic phase of bulk Ca_2RuO_4 and comparable to (or even higher than) that of the insulating phase[35] in the temperature range of the measurements (290–400 K), and the formation of a high-resistivity phase was suggested in this temperature range.

By conducting DC current–voltage measurements for the $Ca_2RuO_4/LaAlO_3$ (001) and $Ca_2RuO_4/NdCaAlO_4$ (100) thin films, significant effects of epitaxial strain on the nonlinear transport properties were experimentally suggested in this study. Fig. 4 shows the current–voltage characteristics of the thin films measured using Ar (100 nm)/Cr (5 nm) in-plane two-terminal electrodes under current-sweeping conditions in a temperature range of 20–590 K. For the $Ca_2RuO_4/NdGaO_3$ (110) thin films, rather leaky current-transport characteristics, which would be extrinsically influenced by the contributions from the interfacial reactant layer, were observed in the current–voltage measurements under high voltages. We thus excluded the characteristics of the $Ca_2RuO_4/NdGaO_3$ (110) thin films from Fig. 4 in this paper and discussed the mechanisms of the nonlinear transport properties without considering these characteristics. As Fig. 4(a) shows, significant nonlinearity and NDR behavior, expected to be caused by the current-induced transition,[21] were demonstrated in the current–voltage characteristics of the $Ca_2RuO_4/LaAlO_3$ (001) thin films for T < 240 K. In clear contrast, the phase-transition-based transport nonlinearity of Ca_2RuO_4 was largely diminished in the [100]-oriented $Ca_2RuO_4/NdCaAlO_4$ (100) thin films in the current–voltage measurements. Figs. 4(b) and 4(c) show the current–voltage characteristics of the $Ca_2RuO_4/NdCaAlO_4$ (100) thin films measured in the [1−10] and [001] directions, respectively. As the figures indicate, the current–voltage characteristics of the thin films were almost linear in both the [1−10] and [001] directions, unlike $Ca_2RuO_4/LaAlO_3$ (001), and no sign of NDR behavior was observed in the characteristics for <590 K. In Fig. 5, double logarithmic plots of the current–voltage characteristics are shown for the $Ca_2RuO_4/LaAlO_3$ (001) and $Ca_2RuO_4/NdCaAlO_4$ (100) thin films. We can understand from the plots that the transport characteristics of the $Ca_2RuO_4/NdCaAlO_4$ (100) thin films in the [001] direction are almost completely linear ($I \propto V^1$) over the measurement range of 30 mV–30 V, while the characteristics of the $Ca_2RuO_4/LaAlO_3$ (001) thin films

have almost no linear part in the profiles over the voltage range of 70 mV–30 V even in the low current region around 10^{-5} A. Therefore, the measurements directly indicate a significant difference in the transport nonlinearity between the $Ca_2RuO_4/LaAlO_3$ (001) and $Ca_2RuO_4/NdCaAlO_4$ (100) thin films, which is attributable to the difference in the epitaxial strain states.

If the $Ca_2RuO_4/NdCaAlO_4$ (100) thin films have a significantly smaller TCR (in amplitude) than the $Ca_2RuO_4/LaAlO_3$ (001) thin films in the temperature ranges of the current–voltage measurements, then the difference in the transport nonlinearity may be explained based on the difference in the TCR. As demonstrated in conventional band semiconductor materials without a metal–insulator transition,[7] if the TCR is significantly smaller, then the temperature increase induced by Joule self-heating will cause a smaller amount of resistivity decrease in Ca_2RuO_4 even without assuming the current-driven transition, and the transport nonlinearity due to the resistivity decrease may be significantly diminished. However, this Joule-heating-based mechanism for nonlinear transport properties is experimentally refuted in $Ca_2RuO_4/NdCaAlO_4$ (100) thin films. We plot the TCR values extracted from the current–voltage characteristics of the $Ca_2RuO_4/NdCaAlO_4$ (100) thin films (Figs. 4(b) and 4(c), using the resistance values read at 1.0 μA) in Fig. 3(b). As shown in this figure, the $Ca_2RuO_4/NdCaAlO_4$ (100) thin films under the measurement conditions have a finite TCR of 0.5–4% in the temperature range of 400–590 K, which is comparable to that in the $Ca_2RuO_4/LaAlO_3$ (001) thin films under the current–voltage measurement conditions. Therefore, these characteristics suggest that the difference in the transport nonlinearity between the $Ca_2RuO_4/LaAlO_3$ (001) and $Ca_2RuO_4/NdCaAlO_4$ (100) thin films does not originate in the resistivity changes induced by Joule heating but is based on intrinsic properties of the current-induced phase transition.

As a possible scenario for the observations, we can assume that the difference in the transport nonlinearity is caused by the difference in the film orientations of the $Ca_2RuO_4/LaAlO_3$ (001) and $Ca_2RuO_4/NdCaAlO_4$ (100) thin films when the lattice dimension changes in the nonlinear transport phenomena are considered for the thin-film structures. For the NDR-type nonlinear transport properties of bulk Ca_2RuO_4, the large change in the lattice dimensions has been demonstrated to be mainly caused in the *c*-axis direction of Ca_2RuO_4 depending on the current density, in contrast to the nearly stable *a*-axis length and relatively small changes in the *b*-axis length in the crystal structures.[10,25] When the changes in the crystal lattice dimensions are assumed for the epitaxial films, we can expect that bulk-like large changes in the *c*-axis dimension will be permitted in the

$Ca_2RuO_4/LaAlO_3$ (001) thin films, as these films have no lattice matching in the out-of-plane [001] direction (Fig. 2(e)). However, the changes in the *c*-axis dimension and resultant energy gap suppression in Ca_2RuO_4[6] will be strongly inhibited in the $Ca_2RuO_4/NdCaAlO_4$ (100) thin films, which have direct crystal lattice matching with the substrate in the in-plane [001] direction (Fig. 2(f)). Therefore, considering the mechanisms reported for bulk Ca_2RuO_4, the progression of the current-induced transition is assumed to be significantly suppressed in the [110]-oriented $Ca_2RuO_4/NdCaAlO_4$ (100) thin films by the strain, and the transport nonlinearity may be diminished by the suppression of the current-driven transition.

4. Conclusions

Through growth of Ca_2RuO_4 epitaxial thin films on various single-crystal substrates by solid-phase epitaxy under nonvacuum conditions, the effects of epitaxial strain on the nonlinear transport properties of Ca_2RuO_4 were investigated. Due to the chemical stability against interfacial reactions with Ca_2RuO_4, nearly phase-pure epitaxial growth of Ca_2RuO_4 was demonstrated on $LaAlO_3$ (001), $NdGaO_3$ (110), and $NdCaAlO_4$ (100) substrates among the substrate materials tested in this study. For the Ca_2RuO_4 thin films on $NdCaAlO_4$ (100) substrates, [110]-oriented growth of Ca_2RuO_4 was indicated by XRD measurements, in contrast to the [001]-oriented growth in the $Ca_2RuO_4/LaAlO_3$ (001) and $Ca_2RuO_4/NdGaO_3$ (110) thin films. The $Ca_2RuO_4/NdCaAlO_4$ (100) thin films were also shown to have anisotropic lattice matching with the substrates, where lattice matching was selectively caused in the [001] in-plane direction with lattice relaxation in the [1−10] direction. Being affected by the epitaxial strain states, a difference of more than two orders of magnitude in the resistivity was observed between the $Ca_2RuO_4/LaAlO_3$ (001) thin films (with *ab*-plane tetragonal compression of Ca_2RuO_4) and the $Ca_2RuO_4/NdGaO_3$ (110) and $Ca_2RuO_4/NdCaAlO_4$ (100) thin films (with *c*-axis compression of Ca_2RuO_4). Moreover, significant effects of epitaxial strain on the nonlinear transport properties were demonstrated in two-terminal current–voltage measurements of the thin films. In clear contrast to the NDR characteristics observed in the $Ca_2RuO_4/LaAlO_3$ (001) thin films, no significant transport nonlinearity was observed in the current–voltage characteristics of the $Ca_2RuO_4/NdCaAlO_4$ (100) thin films with the [110] orientation. From these results, new insights into the control of nonlinear transport properties in strongly correlated materials were provided, with future applications in Mott computing devices.

Acknowledgments

This work was financially supported by the Suhara Memorial Foundation, the Asahi Glass Foundation, a Grant for Basic Science Research Projects from the Sumitomo Foundation (No. 2200218), the Japan Society for the Promotion of Science (JSPS, KAKENHI No. 23K03919) organized by the Ministry of Education, Culture, Sports, Science, and Technology (MEXT), Japan, and the Hokkaido University Ambitious Doctoral Fellowship (Information Science and AI). Part of this work was conducted under the Advanced Research Infrastructure for Materials and Nanotechnology (ARIM, No. JPMXP1223HK0004) by MEXT at the Open Facility, Global Facility Center, Creative Research Institution, Hokkaido University and the Collaborative Research Projects of Laboratory for Materials and Structures, Institute of Innovative Research, Tokyo Institute of Technology.

References

1) Y. Zhou and S. Ramanathan, Proc. IEEE. **103**, 1289 (2015).
2) Y. Wang, K.-M. Kang, M. Kim, H.-S. Lee, R. Waser, D. Wouters, R. Dittmann, J. J. Yang, and H.-H. Park, Mater. Today. **28**, 63 (2019).
3) T. Nakano and I. Terasaki, Phys. Rev. B. **73**, 195106 (2006).
4) Y. W. Lee, B. J. Kim, J. W. Lim, S. J. Yun, S. Choi, B. G. Chae, G. Kim, and H. T. Kim, Appl. Phys. Lett. **92**, 162903 (2008).
5) F. Nakamura, M. Sakaki, Y. Yamanaka, S. Tamaru, T. Suzuki, and Y. Maeno, Sci. Rep **3**, 2536 (2013).
6) R. Okazaki, Y. Nishina, Y. Yasui, F. Nakamura, T. Suzuki and I. Terasaki, J. Phys. Soc. Jpn, **82**, 103702 (2013).
7) S. Kumar and R. S. Williams, Nat. Commun. **9**, 2030 (2018).
8) W. Yi, K. K. Tsang, S. K. Lam, X. Bai, J. A. Crowell, and E. A. Flores, Nat. Commun. **9**, 4661 (2018).
9) J. Zhang, A. S. McLeod, Q. Han, X. Chen, H. A. Bechtel, Z. Yao, S. N. G. Corder, T. Ciavatti, T. H. Tao, M. Aronson, G. L. Carr, M. C. Martin, C. Sow, S. Yonezawa, F. Nakamura, I. Terasaki, D. N. Basov, A. J. Millis, Y. Maeno, and M. Liu, Phys. Rev. X. **9**, 011032 (2019).
10) C. Cirillo, V. Granata, G. Avallone, R. Fittipaldi, C. Attanasio, A. Avella, and A. Vecchione, Phys. Rev. B. **100**, 235142 (2019).
11) A. Rana, C. Li, G. Koster, and H. Hilgenkamp, Sci. Rep. **10**, 3293 (2020).
12) A. Tsurumaki-Fukuchi, K. Tsubaki, T. Katase, T. Kamiya, M. Arita, and Y. Takahashi, ACS Appl. Mater. Interfaces. **12**, 28368 (2020).
13) K. Jenni, F. Wirth, K. Dietrich, L. Berger, Y. Sidis, S. Kunkemöller, C. P. Grams, D. I. Khomskii, J. Hemberger, and M. Braden, Phys. Rev. Mater. **4**, 085001 (2020).
14) G. Mattoni, S. Yonezawa, F. Nakamura, and Y. Maeno, Phys. Rev. Mater. **4**, 114414 (2020).
15) G. Avallone, R. Fermin, K. Lahabi, V. Granata, R. Fittipaldi, C. Cirillo, C. Attanasio, A. Vecchione, and J. Aarts, npj Quantum Mater, **6**, 91 (2021).
16) C. Adda, M.-H. Lee, Y. Kalcheim, P. Salev, R. Rocco, N. M. Vargas, N. Ghazikhanian, C.-P. Li, G. Albright, M. Rozenberg, and I. K. Schuller, Phys. Rev. X. **12**, 011025 (2022).
17) P. Schofield, A. Bradicich, R. M. Gurrola, Y. Zhang, T. D. Brown, M. Pharr, P. J. Shamberger, and S. Banerjee, Adv. Mater. 2205294 (2022).
18) S. K. Das, S. K. Nandi, C. V. Marquez, A. Rúa, M. Uenuma, E. Puyoo, S. K. Nath, D.

Albertini, N. Baboux, T. Lu, Y. Liu, T. Haeger, R. Heiderhoff, T. Riedl, T. Ratcliff, and R. G. Elliman, Adv. Mater. **35**, 2208477 (2023).

19) T. Luibrand, A. Bercher, R. Rocco, F. Tahouni-Bonab, L. Varbaro, C. W. Rischau, C. Domínguez, Y. Zhou, W. Luo, S. Bag, L. Fratino, R. Kleiner, S. Gariglio, D. Koelle, J.-M. Triscone, M. J. Rozenberg, A. B. Kuzmenko, S. Guénon, and J. del Valle, Phys. Rev. Res. **5**, 013108 (2023).
20) S. M. Bohaichuk, S. Kumar, M. Islam, M. M. Rojo, R. S. Williams, G. Pitner, J. Jeong, M. G. Samant, S. S. P. Parkin, and E. Pop, Phys. Rev. Appl. **19**, 044028 (2023).
21) K. Tsubaki, A. Tsurumaki-Fukuchi, T. Katase, T. Kamiya, M. Arita, and Y. Takahashi, Adv. Electron. Mater. 2201303 (2023).
22) S. Nakamura, Phys. Rev. Lett. **109**, 120602 (2012).
23) F. Peronaci, S. Ameli, S. Takayoshi, A. S. Landsman, and T. Oka, Phys. Rev. B, **107**, 075154 (2023).
24) G. Cao, J. Phys. Condens. Matter, **32**, 423001 (2020).
25) R. Okazaki, K. Kobayashi, R. Kumai, H. Nakao, Y. Murakami, F. Nakamura, H. Taniguchi, and I. Terasaki, J. Phys. Soc. Jpn. **89**, 044710 (2020).
26) X. Wang, Y. Xin, P. A. Stampe, R. J. Kennedy, and J. P. Zheng, Appl. Phys Lett. **85**, 6146 (2004).
27) L. Miao, P. Silwal, X. Zhou, I. Stern, J. Peng, W. Zhang, L. Spinu, Z. Mao, and D. H. Kim, Appl. Phys. Lett. **100**, 052401 (2012).
28) C. Dietl, S. K. Sinha, G. Christiani, Y. Khaydukov, T. Keller, D. Putzky, S. Ibrahimkutty, P. Wochner, G. Logvenov, P. A. van Aken, B. J. Kim, and B. Keimer, Appl. Phys. Lett. **112**, 031902 (2018).
29) C. J. Dietl, Dr. Thesis, Faculty of Mathematics and Physics, University of Stuttgart, Stuttgart (2018).
30) C. S. Chang, M. Holtz, H. Nair, J. Ruf, K. Shen, D. Schlom, and D. Muller, Microsc. Microanal. **24**, 64 (2018).
31) T. Ohnishi, K. Takahashi, M. Nakamura, M. Kawasaki, M. Yoshimoto, and H. Koinuma, Appl. Phys. Lett. **74**, 2531 (1999).
32) A. Biswas, P. B. Rossen, J. Ravichandran, Y.-H. Chu, Y.-W. Lee, C.-H. Yang, R. Ramesh, and Y. H. Jeong, Appl. Phys. Lett. **102**, 051603 (2013).
33) J. Kim, Y. Kim, J. Mun, W. Choi, Y. Chang, J. R. Kim, B. Gil, J. H. Lee, S. Hahn, H. Kim, S. H. Chang, G.-D. Lee, M. Kim, C. Kim, and T. W. Noh, Small Methods. **6**, 2200880 (2022).

34) M. Braden, G. André, S. Nakatsuji, and Y. Maeno, Phys. Rev. B. **58**, 847 (1998).
35) C. S. Alexander, G. Cao, V. Dobrosavljevic, S. McCall, J. E. Crow, E. Lochner, and R. P. Guertin, Phys. Rev. B. **60**, R8422 (1999).
36) O. Friedt, M. Braden, G. André, P. Adelmann, S. Nakatsuji, and Y. Maeno, Phys. Rev. B. **63**, 174432 (2001).

Figure Captions

Table I. Crystal lattice dimensions of bulk Ca_2RuO_4[34,36] and the substrate materials used in this study, lattice mismatches between them, and results of the Ca_2RuO_4 growth trials. In the calculations of the lattice mismatches, [110]-oriented growth of the Ca_2RuO_4 thin film was assumed for the $NdCaAlO_4$ (100) substrate, and [001]-oriented growth was assumed for the other substrates.

Materials	*a* [nm]	*b* [nm]	*c* [nm]	Mismatch [%]	Results
Bulk Ca_2RuO_4 at 295 K	0.383	0.388	1.196	—	—
Bulk Ca_2RuO_4 at 400 K	0.379	0.378	1.226	—	—
$YAlO_3$ (001)	0.366	0.376	0.369	+3.1–+4.4	Ca_2RuO_4 + Impurities
$LaAlO_3$ (001)	0.379	0.379	0.379	+1.0–+2.3	Ca_2RuO_4
$LaSrGaO_4$ (001)	0.384	0.384	1.268	−0.3–+1.1	Impurities (interfacial)
$NdGaO_3$ (110)	0.385	0.386	0.386	−0.5–+0.5	Ca_2RuO_4
LSAT (100)	0.387	0.387	0.387	−1.0–+0.3	Impurities
$NdCaAlO_4$ (100)	0.368	0.368	1.212	−1.3–+5.2	Ca_2RuO_4

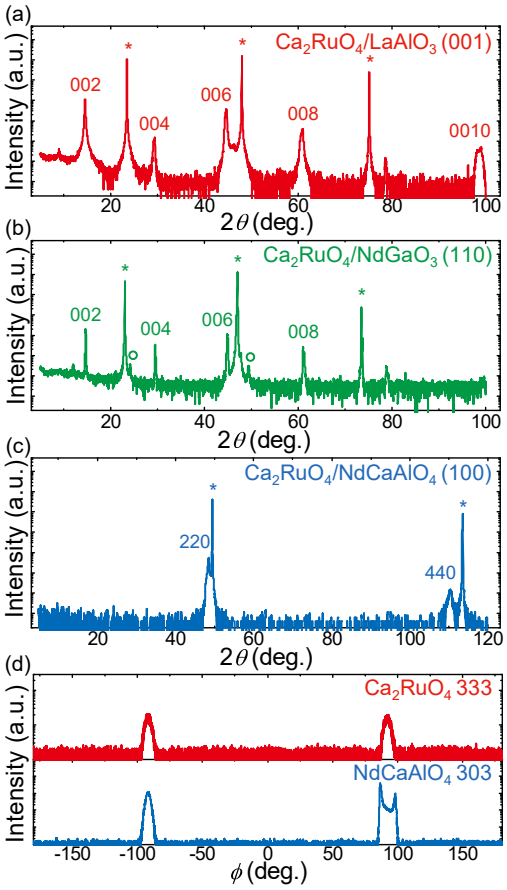


Fig. 1. Out-of-plane XRD patterns measured under a θ–2θ scan for (a) Ca_2RuO_4 (100 nm)/$LaAlO_3$ (001), (b) Ca_2RuO_4 (100 nm)/$NdGaO_3$ (110), and (c) Ca_2RuO_4 (100 nm)/$NaCaAlO_4$ (100) epitaxial thin films. The asterisks in (a–c) indicate the reflections from the substrates. The additional reflection peaks observed in (b) (see main text) are marked by open circles. (d) XRD patterns of a Ca_2RuO_4 (100 nm)/$NaCaAlO_4$ (100) thin film measured under a ϕ scan for the Ca_2RuO_4 333 and $NaCaAlO_4$ 303 reflections.

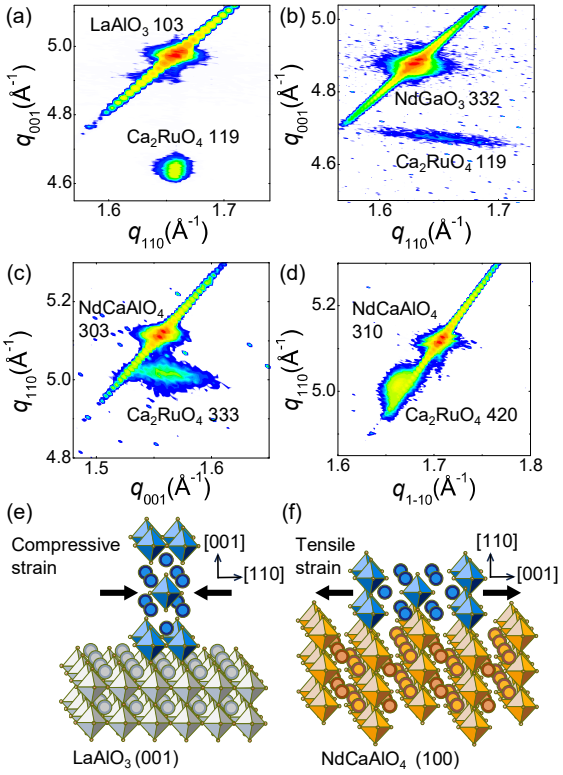


Fig. 2. Reciprocal space maps obtained from the XRD measurements for the Ca_2RuO_4 (100 nm)/$LaAlO_3$ (001), Ca_2RuO_4 (100 nm)/$NdGaO_3$ (110), and Ca_2RuO_4 (100 nm)/$NaCaAlO_4$ (100) thin films around the (a) Ca_2RuO_4 119 and $LaAlO_3$ 103, (b) Ca_2RuO_4 119 and $NdGaO_3$ 332, (c) Ca_2RuO_4 333 and $NaCaAlO_4$ 303, and (d) Ca_2RuO_4 420 and $NaCaAlO_4$ 310 reflections. Indices for the orthorhombic unit cell of Ca_2RuO_4 are used in the axes. Schematic illustrations of the epitaxial relationships and strain states in the (a) Ca_2RuO_4/$LaAlO_3$ (001) and (b) Ca_2RuO_4/$NaCaAlO_4$ (100) thin films. In the illustrations, the formation of the insulating phase of bulk Ca_2RuO_4 is assumed at room temperature.

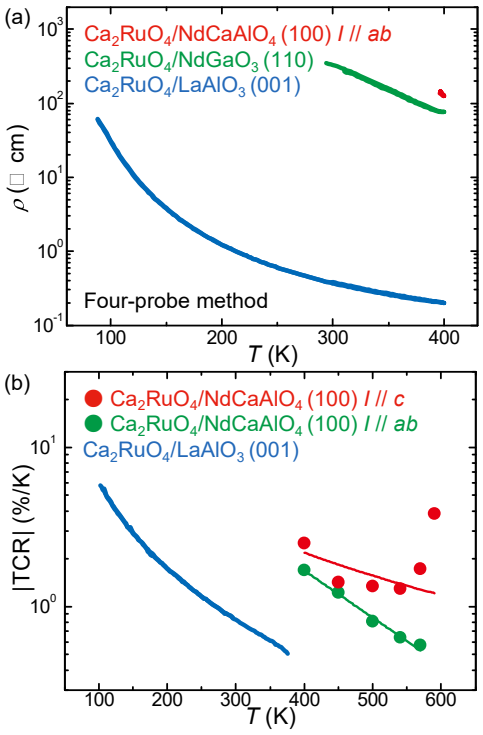


Fig. 3. (a) Temperature dependence of the resistivity measured for the epitaxial films of Ca_2RuO_4 (100 nm)/$LaAlO_3$ (001), Ca_2RuO_4 (100 nm)/$NdGaO_3$ (110), and Ca_2RuO_4 (100 nm)/$NaCaAlO_4$ (100) (with a [1−10] current direction) by the four-probe method. Note that the resistivity of the Ca_2RuO_4 (100 nm)/$NaCaAlO_4$ (100) thin film in the [001] direction was beyond the measurement range of this method because of the resistivity anisotropy of Ca_2RuO_4. (b) Absolute values of the TCR ($|(1/\rho)(d\rho/dT)|$) obtained for the Ca_2RuO_4 (100 nm)/$LaAlO_3$ (001) thin film from the characteristics shown in (a). For comparison, absolute values of the TCR derived from the DC current–voltage characteristics (see text) are also shown in the figure for the Ca_2RuO_4 (100 nm)/$NaCaAlO_4$ (100) thin film.

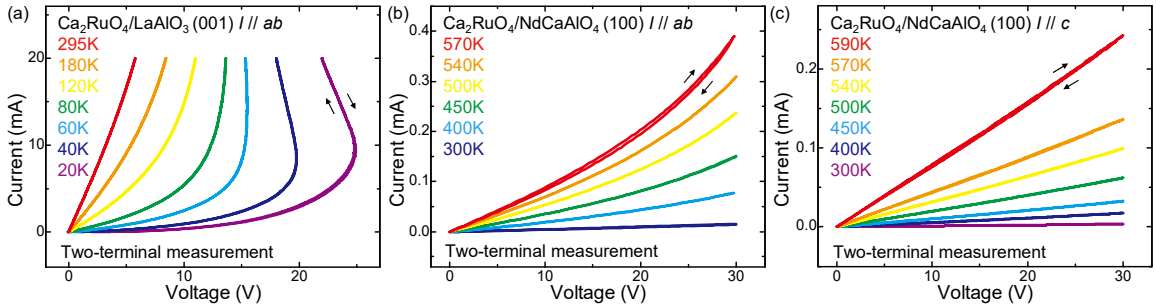


Fig. 4. DC current–voltage characteristics of the (a) Ca_2RuO_4 (100 nm)/$LaAlO_3$ (001) thin film, (b) Ca_2RuO_4 (100 nm)/$NaCaAlO_4$ (100) thin film in the [1−10] direction, and (c) Ca_2RuO_4 (100 nm)/$NaCaAlO_4$ (100) thin film in the [001] direction, measured under current-sweeping conditions at stage temperatures of 20–590 K using Au (100 nm)/Cr (5 nm) two-terminal electrodes. The black arrows in the figures indicate the current-sweeping directions.

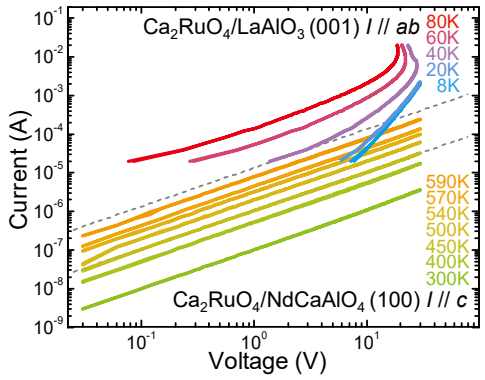


Fig. 5. Double logarithmic plots of the DC current–voltage characteristics of the Ca_2RuO_4 (100 nm)/$LaAlO_3$ (001) thin film and Ca_2RuO_4 (100 nm)/$NaCaAlO_4$ (100) thin film with a [001] current direction, measured at 8–80 K and 300–590 K, respectively. The gray broken lines indicate the results of linear ($I \propto V^1$) fitting for the profiles of the Ca_2RuO_4/$LaAlO_3$ (001) (at T = 40 K) and Ca_2RuO_4/$NaCaAlO_4$ (100) (at T = 450 K) thin films.